Rheol Acta (2004) 44: 80–93
DOI 10.1007/s00397-004-0380-9

ORIGINAL CONTRIBUTION

M. Gregory Forest
Qi Wang
Ruhai Zhou

The flow-phase diagram of Doi-Hess theory for sheared nematic polymers II: finite shear rates

Received: 18 December 2003
Accepted: 6 April 2004
Published online: 30 July 2004

M. G. Forest (✉) · R. Zhou
Department of Mathematics,
University of North Carolina at Chapel Hill, Chapel Hill, NC 27599-3250, USA
E-mail: forest@amath.unc.edu

Q. Wang
Department of Mathematical Sciences,
Florida State University,
Tallahassee, FL 32306, USA

Abstract The purpose of this paper is to extend the rheological predictions of the Doi-Hess kinetic theory for sheared nematic polymers from the anomalous weak shear regime (Forest et al. 2004a) to arbitrary shear rates, and to associate salient rheological and optical properties with the solution space of kinetic theory. Using numerical bifurcation software (AUTO), we provide the phase diagram of all stable monodomain orientational probability distribution functions (PDFs) and their phase transitions (bifurcations) vs nematic concentration (N) and normalized shear rate (Peclet number, Pe) for $Pe \geq 1$. Shear stresses, normal stress differences, the peak direction of the orientational distribution, and birefringence order parameters are calculated and illustrated for each type of PDF attractor: steady flow-aligning, both in and out of the flow deformation plane and along the vorticity axis; unsteady limit cycles, where the peak orientation direction rotates in-plane or around the vorticity axis or in bi-stable orbits tilted between them; and chaotic attractors first observed in kinetic simulations by Grosso et al. (2001). We pay particular attention to correlations between rheological features and the variety of monodomain phase transitions. Together with the weak flow regime, these results provide a nearly complete picture of the rheological consequences of the Doi-Hess kinetic theory for sheared monodomains of rigid, extreme aspect ratio, nematic rods or platelets.

Keyword Nematic polymer · Kinetic · Shear flow · Phase diagram · Rheology

Introduction

In this paper, we extend rheological predictions of the Doi-Hess kinetic theory (Doi 1981; Hess 1976) for sheared nematic polymers from the anomalous weak shear regime (Forest et al. 2004a) to general shear rates, and to associate salient physical properties with nonlinear dynamical systems phenomena. Using numerical bifurcation software AUTO (Doedel et al. 1997), we provide the phase diagram of all stable monodomain orientational probability distribution functions (PDFs) and their phase transitions (bifurcations) vs nematic concentration (N) and normalized shear rate (Peclet number, Pe) for $Pe \geq 1$. Stresses and light scattering features are calculated and illustrated for each type of PDF attractor: steady flow-aligning, both in and out of the flow deformation plane and along the vorticity axis; unsteady limit cycles, where the peak orientation direction rotates in-plane or around the vorticity axis or in bi-stable orbits tilted between them; and chaotic attractors first observed in kinetic simulations by Grosso et al. (2001), and independently discovered in mesoscopic tensor models by Brian Edwards (unpublished) (Forest and Wang 2003;

Rienacker et al. 2002). We pay particular attention to the correlation between rheological features and phase transitions.

Together with the weak flow regime, these results provide a nearly complete picture of the rheological consequences of the Doi kinetic theory for sheared monodomains of rigid, extreme aspect ratio, nematic rods or platelets. From here, experimental studies are poised to make definitive benchmarks of all measurable predictive features of the Doi theory, e.g., we give detailed features of shear stress and normal stress differences across the phase diagram. These predictions serve as a basis to definitively evaluate the Doi-Hess theory, and most importantly, to repair weaknesses while preserving strengths of the Doi mean-field kinetic theory. Seminal results of Faraoni et al. (1999), Grosso et al. (2001), Larson (1990), and Larson and Ottinger (1991) are placed within the context of the full space of steady and unsteady, stable and unstable, invariant distribution functions. Certain general conclusions can be asserted from the existing kinetic theory. Steady alignment is the unique response at sufficiently high Peclet number (*Pe*) for each concentration *N* (flow-alignment), and at sufficiently low *Pe* and high concentrations (vorticity-alignment). In the large (approximately a third) remaining parameter space (*N*, *Pe*), dynamics and complexity of monodomain response governs, including in-plane to out-of-plane transitions, steady to unsteady transitions, frequency-halving cascades of bi-stable out-of-plane kayaking states, multiple attractors with distinct orientational and rheological features, and a considerable parameter domain with chaotic attractors. Nearly all features of the phase diagram are robust to constant vs orientation-dependent rotational diffusivity, with changes only in the precise boundary of each region of fixed number and type of attractor.

Kinetic theory for LCPs of spheroidal molecules

We begin with a brief recall of the problem formulation and results from Forest et al. (2004a). Let $f(\mathbf{m},t)$ be the *orientational probability distribution function* (PDF) for rod-like, rigid, extremely high-aspect-ratio molecules with axis of symmetry $\mathbf{m}$ on the unit sphere S^2. The Smoluchowski equation for $f(\mathbf{m},t)$ in a flow field $\mathbf{v}$ is given by (Doi 1981; Hess 1976)

$$\frac{Df}{Dt} = \mathcal{R}\cdot[D_r(\mathbf{m})(\mathcal{R}f + \frac{1}{kT} f \mathcal{R}V)] - \mathcal{R}\cdot[\mathbf{m}\times\dot{\mathbf{m}}f], \tag{2}$$

$$\dot{\mathbf{m}} = \Omega\cdot\mathbf{m} + [\mathbf{D}\cdot\mathbf{m} - \mathbf{D}:\mathbf{mmm}], \tag{1}$$

where $D_r(\mathbf{m})$ is the rotary diffusivity which we initially hold constant, $D_r(\mathbf{m}) = D_r^0$, consistent with Faraoni et al. (1999), Forest et al. (2004a), and Grosso et al. (2001); k is the Boltzmann constant; T is absolute temperature; $\mathcal{R} = \mathbf{m}\times\frac{\partial}{\partial\mathbf{m}}$ is the rotational gradient operator (Bird et al. 1987); and $\frac{D}{Dt}(\bullet)$ denotes the material derivative $\frac{\partial}{\partial t}(\cdot) + \mathbf{v}\cdot\nabla(\cdot)$. We consider simple shear flow in Cartesian coordinates (x,y,z) with shear rate $\dot{\gamma}$, x is the flow direction, y is the flow-gradient direction, and z is the vorticity axis:

$$\mathbf{v} = \dot{\gamma}(y,0,0)\,; \tag{2}$$

$\mathbf{D}$ and Ω in Eq. (3) are the corresponding rate-of-strain and vorticity tensors:

$$\mathbf{D} = \frac{1}{2}\dot{\gamma}\begin{pmatrix}0&1&0\\1&0&0\\0&0&0\end{pmatrix}, \Omega = \frac{1}{2}\dot{\gamma}\begin{pmatrix}0&1&0\\-1&0&0\\0&0&0\end{pmatrix}. \tag{3}$$

The *Peclet number*, $Pe = \dot{\gamma}/D_r^0$, is the normalized flow-rate parameter. The second-moment of the PDF,

$$\mathbf{M} = \langle\mathbf{mm}\rangle = \int_{\|\mathbf{m}\|=1}\mathbf{mm}\, f\,(\mathbf{m},t)d\mathbf{m}, \tag{4}$$

determines the mean-field, Maier-Saupe excluded-volume potential V,

$$V = -\frac{3}{2}N\,kT\,\mathbf{mm}:\mathbf{M}\,, \tag{5}$$

where N is the dimensionless strength of the potential V, *proportional to the concentration of rods*. All results given here extend to high-aspect-ratio, rigid nematic platelets by a simple symmetry described in Forest et al. (2002). The phase diagrams are identical after one scales out the dependence of D_r^0 on molecule shape. After detailed development of the phase diagram for $D_r(\mathbf{m}) \equiv D_r^0$, we present the analogous phase diagram for orientation-dependent rotary diffusivity, then highlight the overwhelming similarities. The dependence of the phase diagram on molecule aspect ratio requires, in essence, a one-parameter continuation of the results presented here. We have begun those massive numerical studies, analogous to the mesoscopic model study of Forest and Wang (2003), to be reported once a clear picture emerges.

The *mesoscopic orientation tensor* $\mathbf{Q}$ is the traceless part of $\mathbf{M}$,

$$\mathbf{Q} = \mathbf{M} - \tfrac{1}{3}\mathbf{I}\,, \tag{6}$$

which provides the link between the kinetic PDF $f(\mathbf{m},t)$ and rheological measurements of principle directions and degrees of alignment, and of shear stress and normal stress differences. The Appendix gives the formulas for $\mathbf{Q}$ and the stress tensor τ associated with any orbit $f(\mathbf{m},t)$ of the kinetic model (Eq. 3). We refer to Forest et al. (2004a) for the numerical procedure and protocols, and report only the results of an extensive study.

The flow phase diagram for $1 \le Pe \le 10$

For weak shear rates, $0 < Pe < 1$, Forest et al. (2004a) provided a detailed flow-phase diagram. Figure 1 shows the extension of this bifurcation diagram to the parameter regime $1 \le Pe \le 10$, $0 \le N \le 8$. The parameter space divides into 13 distinct regions, labeled I–XIII, where the number and type of attracting distributions are fixed within each region. Table 1 gives the attractor type and multiplicity for each region, whereas Table 2 summarizes the regions where each attractor is found. A summary of the phase transitions that form the boundaries between these regions appears in Table 3. In Tables 4, 5, and 6 we also list the monodomain attractors and phase transitions vs *Pe* for some chosen concentrations.

We now discuss salient features of the flow-phase diagram.

Steady flow-aligning and logrolling states

Regions I and XII cover the majority of (N, Pe) parameter space, wherein the bulk response is *steady and unique*.

Region I is the regime of *flow-alignment in the plane of deformation*, labeled **FA**. All sufficiently dilute concentrations (which are isotropic without flow) lead to simple flow-alignment of the molecular distribution at onset of shear; the effect of increased flow rate is to shift the peak angle of the PDF, called the *Leslie angle* ϕ_L (by analogy with continuum Leslie-Ericksen theory). This macroscopic feature is calculated by first projecting f onto the first five spherical harmonics, which specifies the second-moment tensor $\mathbf{Q}$, Eq. (A2), then computing the eigenvalues $\{d_i - \frac{1}{3}\}_{i=1}^{3}$ and corresponding eigenvectors $\{\mathbf{n}_i\}_{i=1}^{3}$ of $\mathbf{Q}$, from which the largest eigenvalue $d_1 - \frac{1}{3}$ signifies the major director, $\mathbf{n}_1$. *Flow-aligned steady distributions* f_{FA} are characterized by $\mathbf{n}_1^{FA} = \mathbf{n}_1(\mathbf{Q}(f_{FA}))$ of the form

$$\mathbf{n}_1^{FA} = (cos\phi_L, sin\phi_L, 0), \tag{7}$$

where ϕ_L is called the Leslie alignment angle. Figure 2 depicts ϕ_L vs *Pe* for several concentrations: the lowest concentrations $N = 4.6$ and $N = 4.7$ are in the bi-stable range of isotropic and nematic quiescent states, whereas $N = 5.05$, 5.5, 6.4 are nematic concentrations which require increasingly higher shear rates to access Region I. Note that $\phi_L(N, Pe)$ is generally small for *nematic concentrations* and sufficiently high shear rates, $Pe \ge 1$, i.e., the major director orients close to the flow axis; ϕ_L can be *positive or negative*. Even for the concentration $N = 4.6$ (near the quiescent isotropic state), for which $\phi_L \approx 10°$ as Pe $\to 0$, ϕ_L quickly drops toward the flow axis as *Pe* increases.

The degree of alignment, characterized by d_1, and the flow birefringence, characterized by $d_1 - d_3$ and $d_2 - d_3$, of **FA** states are given in Fig. 3. For comparison, the quiescent values of d_1 for $N = 4.6$, 4.7, 5.05, and 5.5 are given as black dots in Fig. 3 along the $Pe = 0$ vertical axis. We observe that the *degree of alignment* for shear-induced flow-aligning states *grows continuously and*

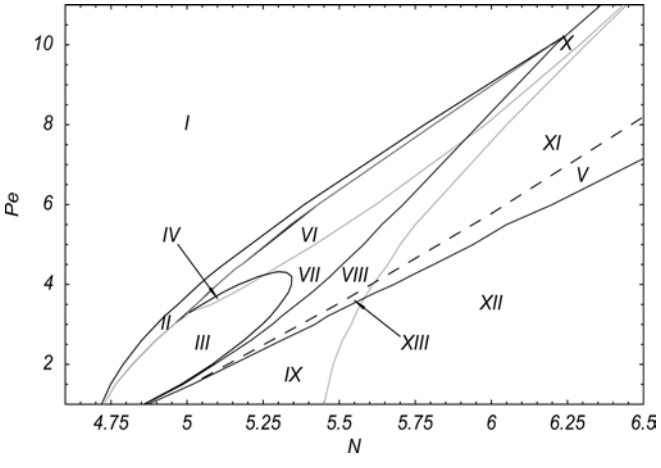

Fig. 1 Bifurcation diagram of all stable states in N, Pe space. Table 1 lists stable state(s) for each region labeled from (I) to (XIII)

Table 1 Attractor transitions for nematic polymers in the region $1 \le Pe \le 12$, $0 < N < 8$. The regions are defined in Fig. 1 and the fixed attractors in each region are listed in Table 1

Region	Attractor type	Multiplicity
I	Flow-aligning (**FA**)	1
II	Out-of-plane steady (**OS**)	2
III	Kayaking 1/Chaos ($\mathbf{K}_1$/**CH**)	2
IV	Chaos (**CH**)	1
V	Tumbling/Log-rolling (**T/LR**)	2
VI	Kayaking 2 ($\mathbf{K}_2$)	2
VII	Kayaking 1/Kayaking 2 ($\mathbf{K}_1$/$\mathbf{K}_2$)	3
VIII	Kayaking 1-Wagging ($\mathbf{K}_1$/**W**)	2
IX	Kayaking 1 ($\mathbf{K}_1$)	1
X	Wagging (**W**)	1
XI	Wagging/Log-rolling (**W/LR**)	2
XII	Log-rolling (**LR**)	1
XIII	Kayaking 1-Tumbling ($\mathbf{K}_1$/**T**)	2

Table 2 Stable states (attractors) and multiplicity for each region in the bifurcation diagram, Fig. 1

Stable attracting states	Region
Flow-aligning (**FA**)	I
Out-of-plane steady (**OS**)	II
Kayaking 1 ($\mathbf{K}_1$)	III, VII, VIII, IX
Chaos (**CH**)	III, IV
Kayaking 2 ($\mathbf{K}_2$)	VI, VII
Tumbling (**T**)	V, XIII
Wagging (**W**)	VIII, X, XI
Log-rolling (**LR**)	IX, XII

Table 3 Parameter regions I–XIII of Fig. 1 where each attractor type is resonated

Boundary (bottom to top)	Bifurcation type	Attractor transition (bottom to top regions)
VI–II	Hopf	$K_2^{+,-}$ to $OS^{+,-}$
IV–VI	Periodic doubling	Chaos to $K_2^{+,-}$
XII–V	Periodic doubling	Unstable to stable**T**, **LR** remains
XII–IX	Hopf	**LR** to $\mathbf{K}_1$
IX–XIII	Periodic doubling	Unstable to stable**T**, $\mathbf{K}_1$ remains
XI–VIII	Hopf	**LR** to $\mathbf{K}_1$, **W** remains
VIII–VII	Transcritical	**TW** to $\mathbf{K}_2$, $\mathbf{K}_1$ remains
VII–VI	Saddle-node	$\mathbf{K_1}$ disappears, stable $K_2^{+,-}$ remain
VIII–X	Saddle-node	$\mathbf{K_1}$ disappears, stable **W** remains
X–I	Hopf	**W** to **FA**
VII–III	Periodic doubling	Stable $K_2^{+,-}$ to chaos
III–IV	Saddle-node	$\mathbf{K_1}$ disappears, chaos continues

Table 4 Monodomain attractors and phase transitions vs shear rate *Pe* at fixed concentration $N = 5.2$, Fig. 1

State	$\mathbf{K_1}$	$\mathbf{K_1/TW}$	$\mathbf{K_1/K_2}$	$\mathbf{K_1/CH}$
Pe Region	(0, 2.17)	(2.17, 2.53)	(2.53, 2.69)	(2.69, 3.99)
State	**CH**	**K**	**OS**	**FA**
Pe Region	(3.99, 4.10)	(4.10, 4.65)	(4.65, 4.98)	(4.98, 10.0)

Table 5 Monodomain attractors and phase transitions vs shear rate *Pe* at fixed concentration $N = 5.5$, Fig. 1

State	**LR**	$\mathbf{K_1}$	$\mathbf{K_1/TW}$	$\mathbf{K_1/K_2}$
Pe Region	(0, 2.33)	(2.33, 3.31)	(3.31, 4.44)	(4.44, 5.38)
State	$\mathbf{K_2}$	**OS**	**FA**	
Pe Region	(5.38, 6.38)	(6.38, 6.60)	(6.60, 10.0)	

Table 6 Monodomain attractors and phase transitions vs shear rate *Pe* at fixed concentration $N = 6$, Fig. 1

State	**LR**	**LR/TW**	$\mathbf{K_1/TW}$	**TW**
Pe Region	(0, 5.22)	(5.22, 7.63)	(7.63, 8.16)	(8.16, 8.33)
State	$\mathbf{K_2}$	**OS**	**FA**	
Pe Region	(8.33, 9.00)	(9.00, 9.07)	(9.07, 10.0)	

rapidly for concentrations near the quiescent isotropic-nematic transition. By contrast, at higher nematic concentrations, there is an initial drop in d_1 from the quiescent value to values shown in Fig. 3. Recall flow-aligning states first occur only above a critical *Pe* vs *N*. Then, d_1 grows slowly as *Pe* increases, requiring very high $Pe \approx 20$ or higher to regain the quiescent value.

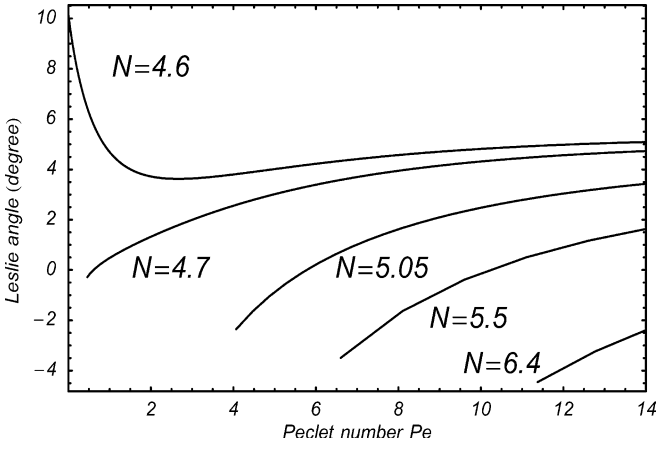

Fig. 2 Leslie angle of the stable flow-aligning states (Region I, Fig. 1) for five different concentrations N

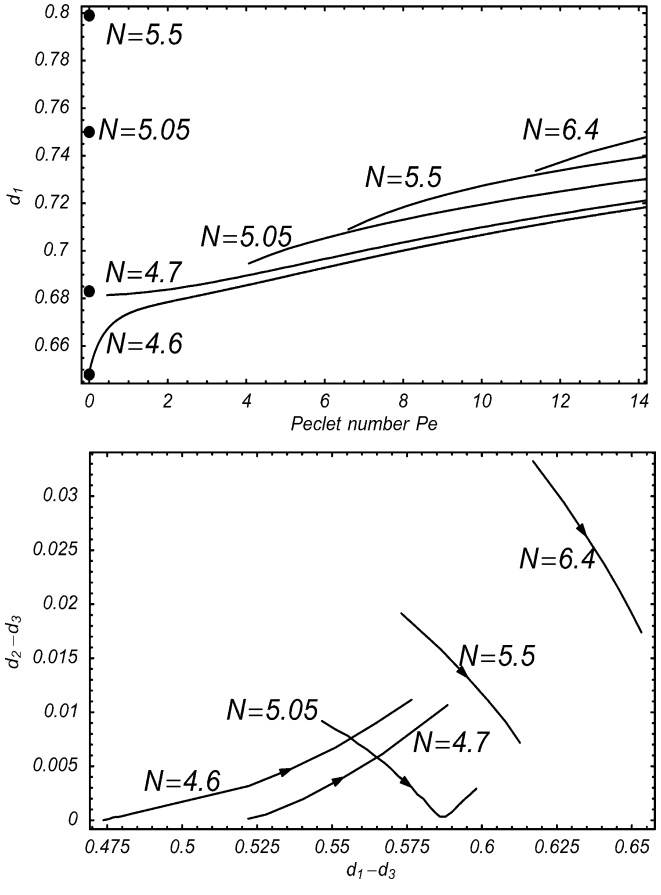

Fig. 3 Order parameters for the stable flow-aligning states. The largest eigenvalue d_1 of the second-order moment M is shown prior to flow (solid dots on the $Pe = 0$ axis), and then in the range of *Pe* with FA attractors at four distinct concentrations $N = 4.6$, 4.7, 5.05, and 5.5. In the *bottom figure*, the maximum birefringence, d_1-d_3, and the degree of biaxiality, d_2-d_3, are computed from M and depicted for the range of *Pe* at each concentration from the *top figure*. *Arrows* in the *bottom figure* indicate increasing *Pe*. The turning point along the curve for $N = 5.05$ indicates passage through a uniaxial state (d_2-d_3)

These results capture tug-of-war for technological applications of nematic polymers in shear-dominated processing flows. By controlling N and Pe in Region I, the flow achieves the goal of selecting the principle alignment direction $\left(\theta = \frac{\pi}{2}, \phi = \phi_L\right)$ which is arbitrary otherwise. However, one sacrifices the strong focusing of the PDF in the quiescent nematic phase and must impose very high shear rates to regain the degree of alignment.

To make these results concrete, we provide the second moment tensor $\mathbf{M}_{\text{theory}}$ derived from the PDF for $N = 5.5$, $Pe = 9.6$ to compare with experimental data on 13.5 wt% PBDG at a shear rate of 100 s^{-1} (Burghardt 1998):

$$\mathbf{M}_{theory} = \begin{pmatrix} 0.726 & -0.004 & 0. \\ -0.004 & 0.144 & 0. \\ 0. & 0. & 0.130 \end{pmatrix}$$

$$\mathbf{M}_{experiment} = \begin{pmatrix} 0.782 & -0.003 & 0. \\ -0.003 & 0.112 & 0. \\ 0. & 0. & 0.106 \end{pmatrix}$$

The theory predicts the Leslie alignment angle is $-0.39°$, while the experiment shows this angle is $-0.26°$. Birefringence parameters d_1-d_3, d_2-d_3 for these two tensors are 0.596, 0.014 and 0.676, 0.006, respectively. Thus, without tortuous parameter fitting, the kinetic theory easily reproduces data in the simplest response Region I of in-plane flow-alignment.

The apparent viscosity (η), first (N_1) and second (N_2) normal stress differences of **FA** states for nematic concentrations across Region I are computed in Fig. 4 and represented as filled Δs (which also connects these properties to different attractors in neighboring regions). One observation is that, at the birth of the **FA** states at a critical Pe for each N, the first normal stress difference is negative ($N_1 < 0$), then N_1 grows with Pe, reaching positive values for $N = 5.05$, but remaining negative out to $Pe = 10$ for high concentrations. For fixed N and sufficiently large Pe, N_1 becomes positive. N_2 remains sufficiently close to zero to be experimentally negligible, whereas the apparent viscosity thins on the order of 10% over the Pe range given.

Region XII is the *logrolling* (**LR**) regime, characterized by major director $\mathbf{n}_1$ *aligned with the vorticity axis*, $\mathbf{n}_1 = (0,0,1)$. This is the unique response for sufficiently high concentrations and sufficiently weak flow rates. The explicit constraints are given numerically by the two bifurcation curves of Fig. 1 that form the boundary of Region XII with Regions IX and XI, respectively. The **LR** attractor persists into Regions XI and V, where it coexists with an in-plane, stable periodic PDF called tumbling (**T**) or wagging (**W**), which we discuss later.

The degrees of alignment, flow birefringence, and stress predictions for the **LR** states of Regions XII, XI, V are provided in Figs. 5 and 6. One concludes that

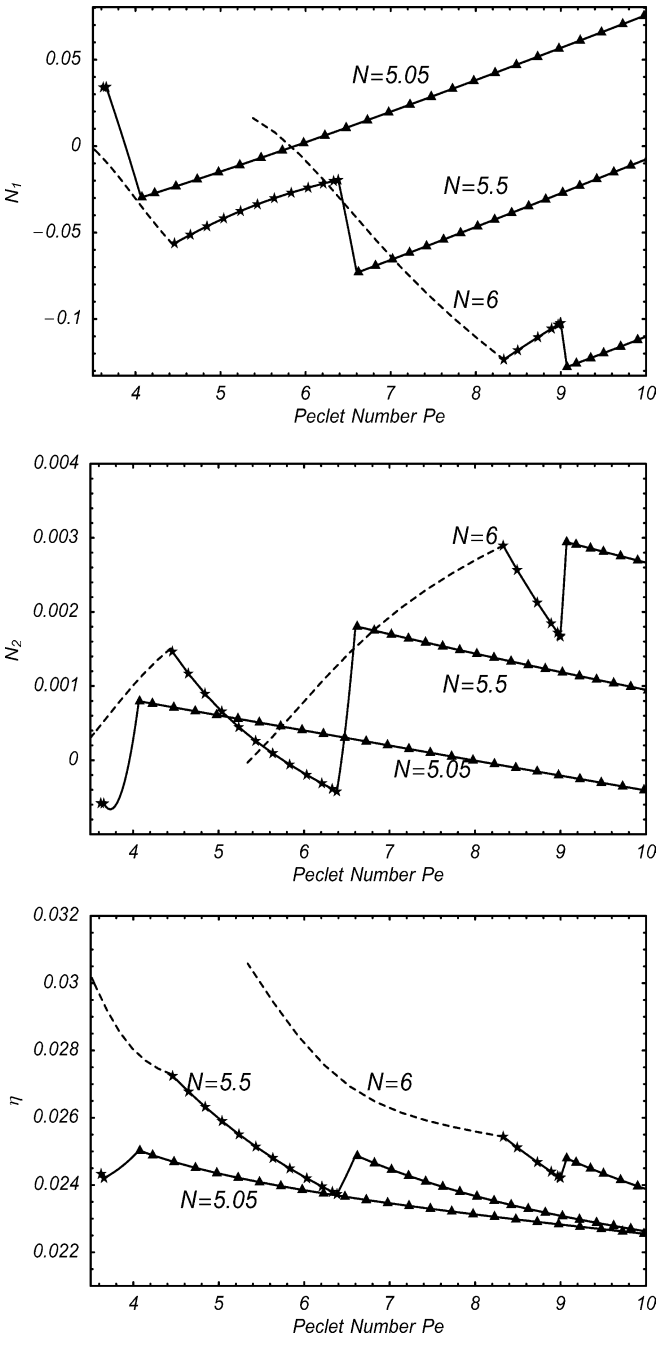

Fig. 4 Normal stress differences and apparent viscosity for several vertical slices of Fig. 1. The fonts label different attractor type: Dashed line (–) for TW, stars (*) for tilted kayaking $\mathbf{K}_2^{\pm}$, solid line (–) for $OS^{\pm}$, and filled triangles (▲) for FA

increasing flow rate leads to greater biaxiality (d_2-d_3 increases) yet *lower maximum degree of orientation* (d_1 decreases), and after an initial gain in maximum flow birefringence (d_1-d_3 increases for $0 < Pe < 1$), an increase in flow rate reduces d_1-d_3 until the unsteady transition to Region VIII or XIII where **LR** bifurcates into a kayaking orbit. Contrary to the **FA** Region I, once the

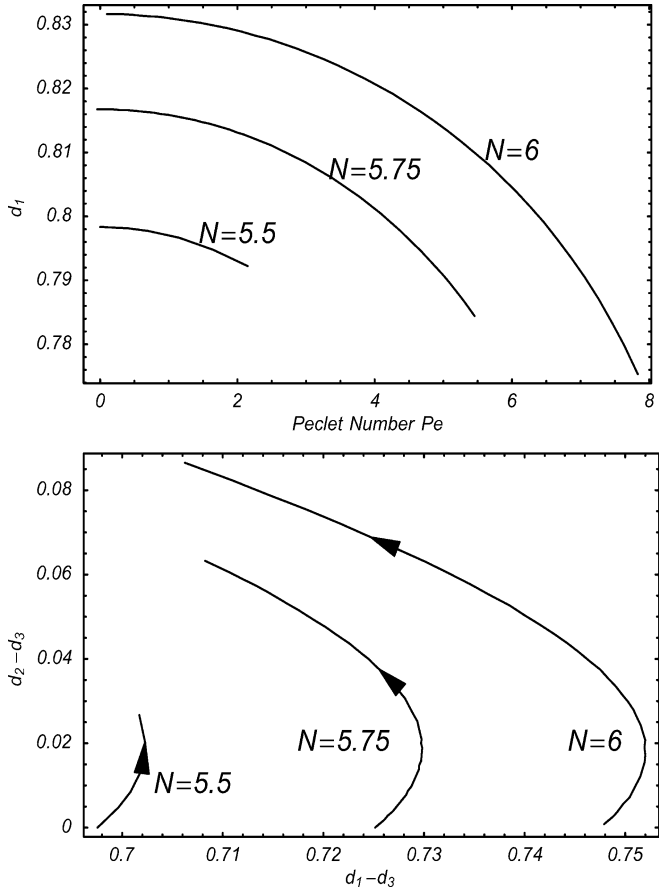

Fig. 5 Order parameters for the stable LR states. The *top figure* depicts the largest eigenvalues d_1 of the second-moment tensor M. The *bottom figure* depicts the maximum birefringence d_1-d_3 and the biaxiality parameter d_2-d_3, which starts at $d_2-d_3=0$ since all nematic equilibria ($Pe=0$) are uniaxial. Arrows in the bottom figure indicate the direction of increasing Pe

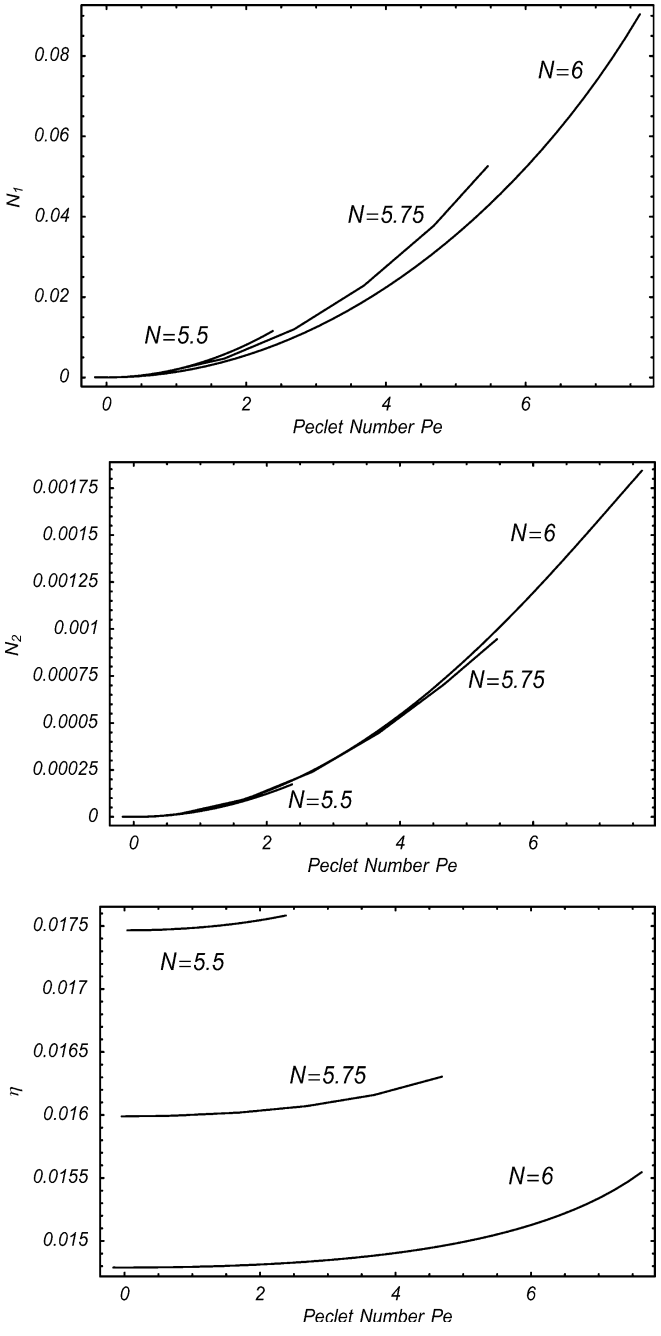

Fig. 6 Normal stress differences and apparent viscosity for the LR stable states of Fig. 5

LR regime is accessed and orientational degeneracy has been broken in favor of the vorticity axis, it is *preferable to lower shear rate in order to recapture the quiescent degree of molecular alignment*.

For **LR** states, the normal stress differences N_1 and N_2 are both positive, increasing functions of N and Pe across Regions XII, XI. The apparent viscosity η shows no dramatic features, dropping slightly at higher concentrations, and growing very slightly for increased Pe at fixed N.

Region II: stable out-of-plane steady states

Stable out-of-plane steady states $OS^{\pm}$ exist only in a narrow parameter band (Region II). If we fix the concentration and decrease the Peclet number, they arise in *pairs* through a symmetric pitchfork bifurcation of the in-plane **FA** state, and disappear through a Hopf bifurcation when a pair of stable tilted kayaking ($\mathbf{K}_2$) orbits emerge, discussed later. For N near 4.7, $OS^{\pm}$ states may coexist with a K_1 stable state for small Pe (Forest et al. 2004a). However, when N is away from 4.7, $OS^{\pm}$ are the only stable states in Region II. For sufficiently large $N>6.24$ or sufficiently large $Pe>10.1$, these states do not exist.

These mirror-symmetric states may be considered to be anomalous, and perhaps unphysical and merely an

artifact of the theory. *However*, they occur in kinetic and mesoscopic models whenever the "tilted kayaking" states $\mathbf{K}_2^{\pm}$ exist. From a fundamental physics perspective, these $OS^{\pm}$ states are important for two reasons. They *connect* the in-plane **FA** steady response *continuously* to the out-of-plane, tilted kayaking response, $\mathbf{K}_2^{\pm}$. *Their existence implies the in-plane steady to out-of-plane unsteady transition is a second-order (continuous) phase transition*. Furthermore, as transition states to $\mathbf{K}_2^{\pm}$ attractors, the $OS^{\pm}$ states are thus far always present nearby the regime of chaotic response.

When the out-of-plane stable steady states first occur in weak shear near $N = 4.7$, the spherical polar angle (between the vorticity axis and the flow deformation plane) of the steady state on either side of the shear plane continuously spans from $\frac{\pi}{2}$ to almost 0 or π in a very narrow interval of Pe (Forest et al. 2004). As N increases, the range vs Pe of the steady polar angle shrinks gradually; when the stable $OS^{\pm}$ states disappear at $N = 6.24$, the polar angle limits to a single value $\frac{\pi}{2}$, where transition from $\mathbf{OS}^{\pm}$ to **FA** states occurs. This phenomenon is depicted in Fig. 7. It also shows that the azimuthal angle of $OS^{\pm}$ steady states is always negative, between 0° and 5°, meaning the major director is close to the flow-vorticity (x-z) plane. Using the kayaking imagery, the paddle (major director) remains at a very shallow depth.

The normalized normal stress differences N_1, N_2, and the shear stress η for stable out-of-plane steady states are plotted in Fig. 8, as well as in Fig. 4 for comparison with other stable states. The signs of N_1 and N_2 are *not* definite, and can be continuously switched by varying either N or Pe. Along the $OS^{\pm}$ states, for fixed N and increasing Pe, N_1 decreases, while N_1 and η increase as the major director swings steadily out-of-plane preparing to begin the $\mathbf{K}_2^{\pm}$ oscillatory response. These features are likely beyond experimental resolution. The most salient observations arise from Figs. 4 and 8. At the pitchfork bifurcation from $OS^{\pm}$ to **FA** stable states, N_1 attains a local minimum, while N_2 and the shear stress η attain local maxima. At the other boundary of Region II, the Hopf bifurcations from $OS^{\pm}$ to $\mathbf{K}_2^{\pm}$, N_1 attains a maximum, and N_2 and η attain minima.

Thus the $\boldsymbol{OS}^{\pm}$ *emergence and disappearance are associated not with sign changes of* N_1, N_2, *but with local maxima or minima of stress features*!

Stable tumbling and wagging states

The largest wedge-shaped parameter region of VIII, X, XI, XIII, V in Fig. 1 has stable in-plane, oscillatory states called tumbling (**T**, in Regions XIII, V) and wagging (**W**, in Regions VIII, X, XI). Either **T** or **W** is the unique attractor only in Region X, bistable in Region VIII, XIII with out-of-plane $\mathbf{K}_1$ orbits, and bistable in Region XI, V with steady **LR** states.

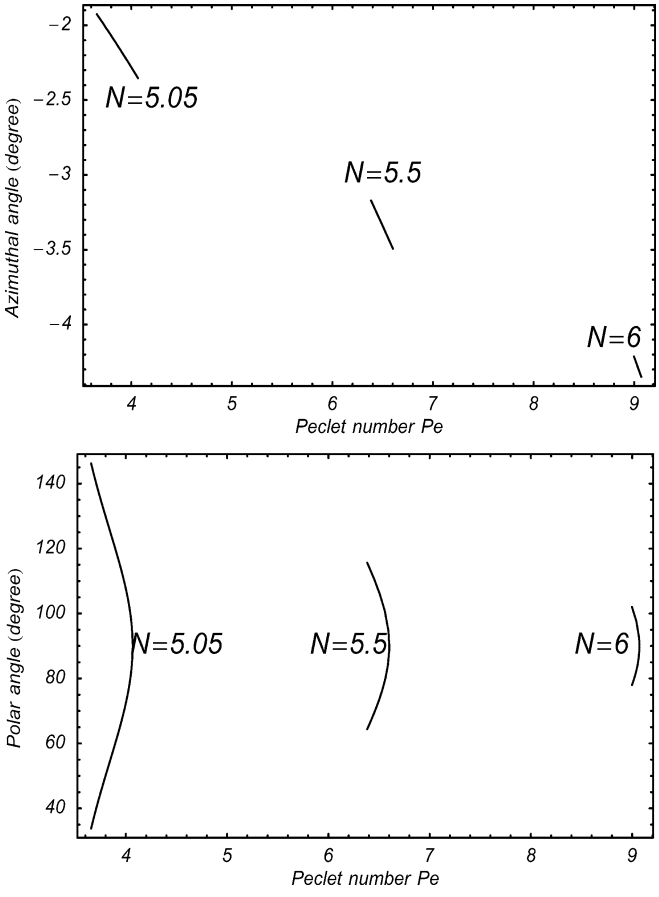

Fig. 7 Azimuthal (in-plane) angle and polar angle of the major director for the symmetric pair of out-of-plane stable steady states, $OS^{\pm}$. The polar angle is measured from the vorticity (z) axis to the shearing plane, and the azimuthal angle is measured counterclockwise from the flow axis. The bistable states OS^{+}, OS^{-} are mirror symmetries of each other, with equal azimuthal angle and polar angle ϕ and $180°-\phi$

We note further that **T** states exist in the lower Pe regions IX and XII, but they are *unstable* to arbitrary out-of-plane perturbations. We refer to Forest et al. (2004a) for details. From Fig. 1, **T**/**W** attractors exist in a range of Pe, $Pe^L < Pe < Pe^U$, for each $N > 4.75$, where Pe^L and Pe^U increase vs N, forming regions VIII, X, XI, XIII and V. The key bifurcations to understand can be described by fixing $N > 4.75$, and finding the lower and upper values of Pe with **T**/**W** attractors. A typical slice of *all* stable and unstable solutions vs Pe is given by the bifurcation diagram for $N = 5.5$ given in Fig. 9. **T** attractors arise through an instability-stability transition due to collision of unstable **T** and unstable $\mathbf{K}_1$ branches. The **T**–**W** transition occurs typically along the stable branch. The **W** orbit then destabilizes through an out-of-plane transition to a pair of $K_2^{\pm}$ states.

Tumbling or wagging periodic distributions can be characterized as follows by computing the major director $\mathbf{n}_1$ of the second-moment **Q** of the PDF:

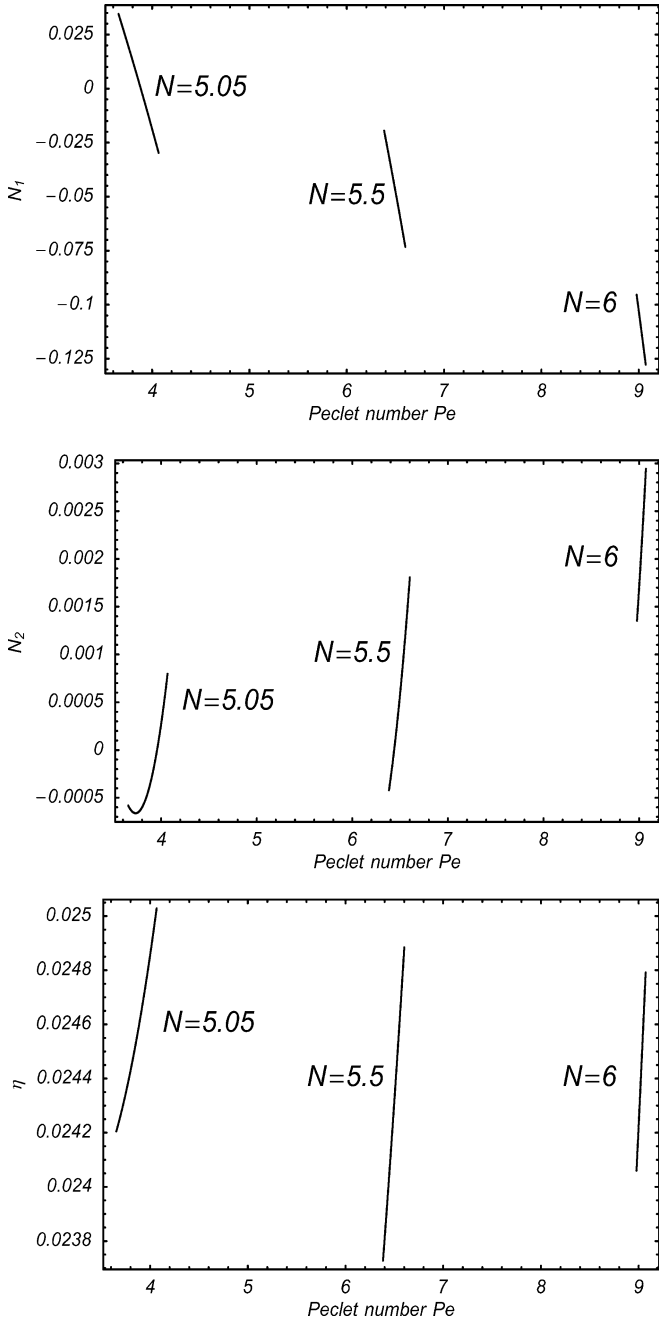

Fig. 8 First and second normal stress differences and apparent viscosity for the OS$^{\pm}$ stable steady states of Fig. 7

$$\mathbf{n}_1(\mathbf{Q}(f(\mathbf{m},t))) = (cos\phi(t), sin\phi(t), 0)\,, \tag{8}$$

where the angle $\phi(t)$ of the director $\mathbf{n}_1$ is monotone for tumbling orbits and oscillates in a finite range for wagging orbits. Figure 10 shows the angles for two wagging states with parameters $N = 5.5$ and $Pe = 3.56$, 4, respectively. One observes larger amplitudes of oscillation as the **W**–**T** transition is approached, along with a compressed timescale of director resetting from minimum to maximum angle. The transition from tumbling to wagging states is around $Pe = 3.55$.

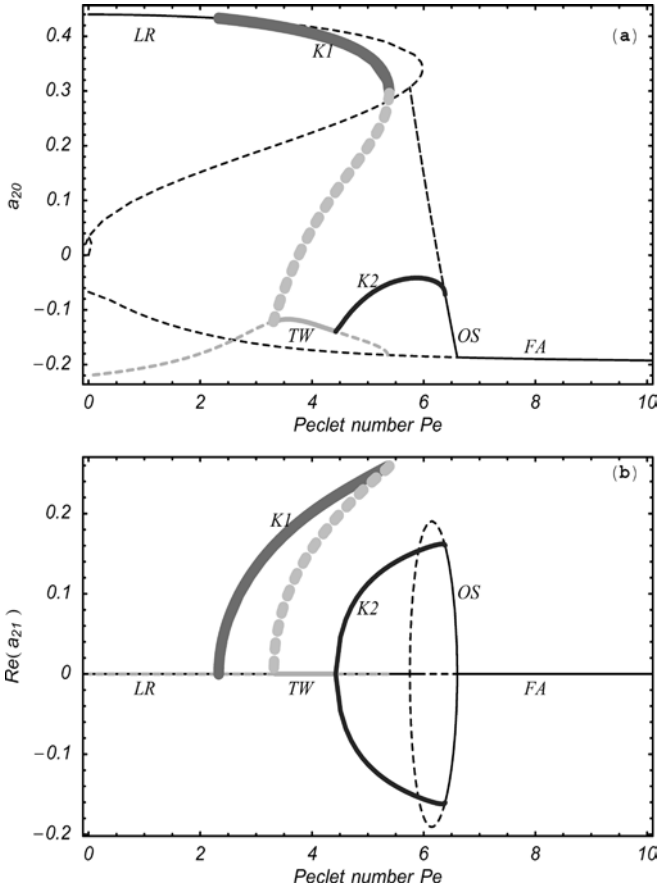

Fig. 9 A detailed bifurcation diagram of unstable (*dashed*) and stable (*solid*) monodomain PDFs vs *Pe* for fixed concentration $N = 5.5$. The transition sequence vs *Pe* is given in Table 5

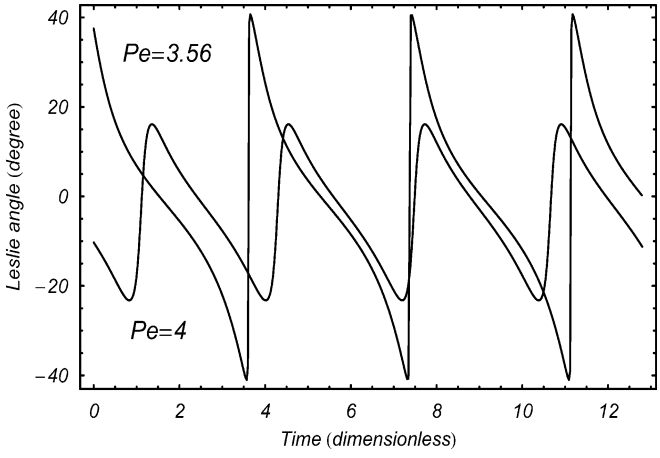

Fig. 10 Dynamics of the Leslie angle computed from the major director of the PDF along the W branch of attractors in Fig. 9, for two shear rates $Pe = 3.56$ and 4.0. Note the maximum amplitude contracts as *Pe* increases

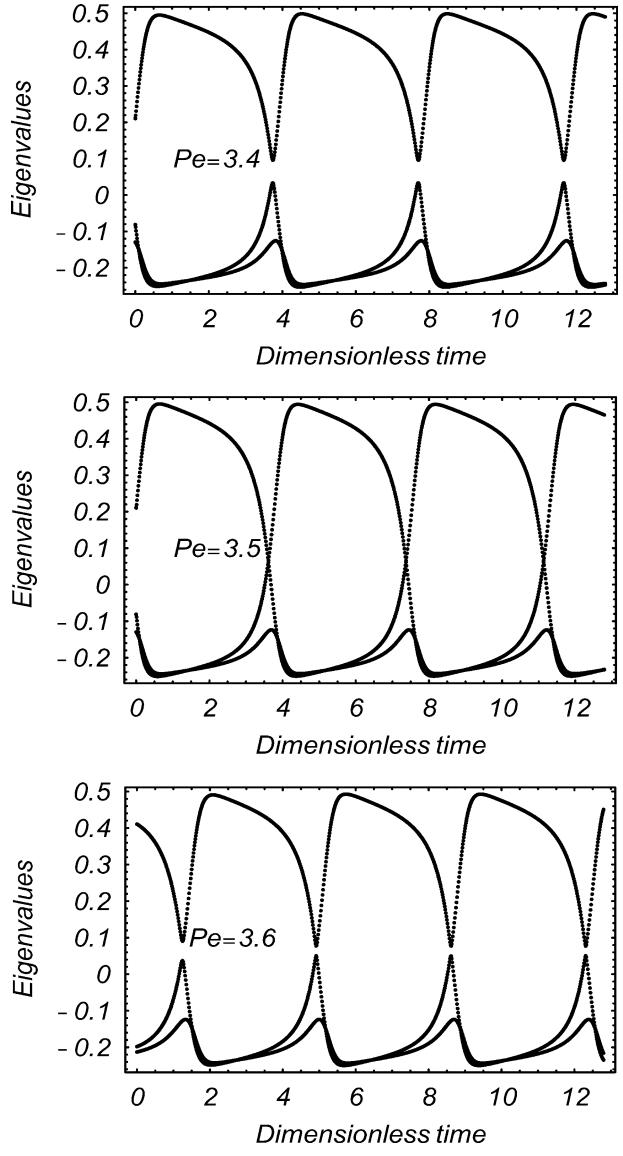

Fig. 11 Transient passage through defect states and the T-W transition. Eigenvalues of the second moment tensor $Q(f)$ for $N = 5.5$ and three different Peclet numbers. *Top figure*: T attractor for $Pe = 3.40$. *Middle figure*: T-W transition for $Pe = 3.55$. *Bottom figure*: W attractor for $Pe = 3.60$. The largest eigenvalue remains simple during the T and W limit circles, so that the major director is always uniquely defined. However, the limit cycle near the T-W transition leads to a multiple largest eigenvalues, where the major director is degenerate

Figure 11 shows the three eigenvalues of the second moment tensor **Q** during the transition between tumbling and wagging. We conclude that, at the transition point, the periodic states pass through the defect state (the two largest eigenvalues are the same, so the major director is not uniquely defined), while for both tumbling and wagging states, the largest eigenvalue remains simple.

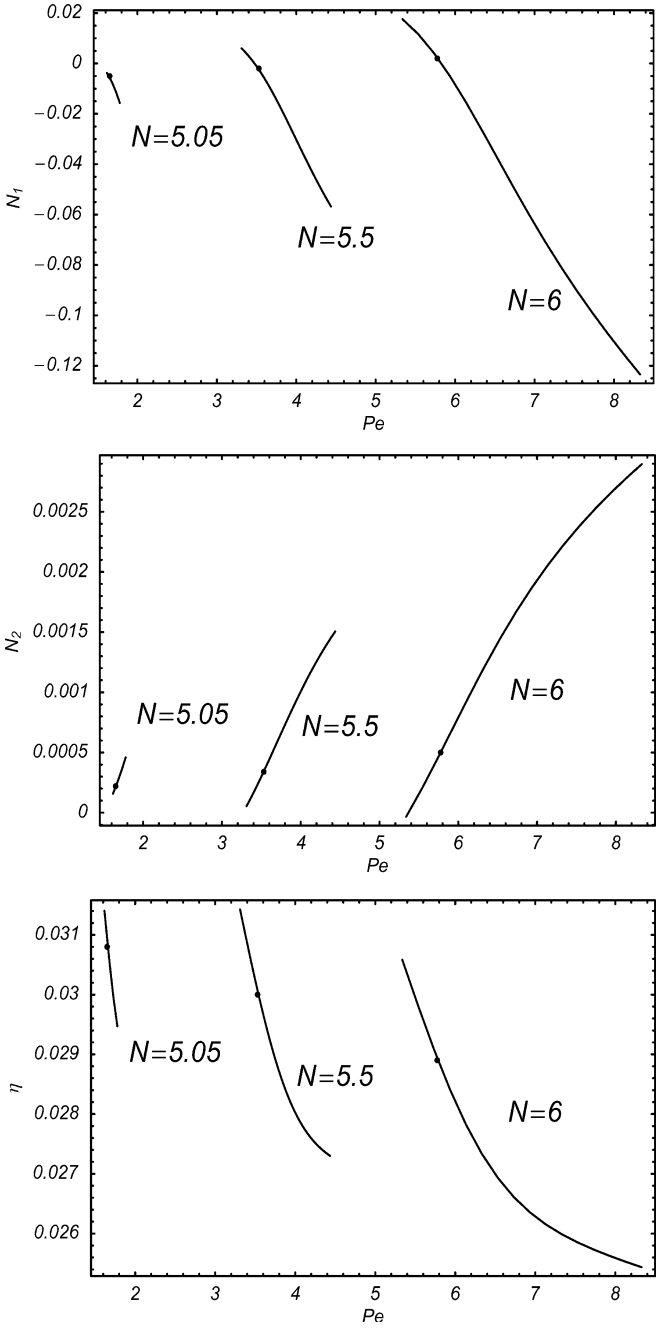

Fig. 12 Average normal stress differences and apparent viscosity for tumbling/wagging stable states of Regions VIII, X, XI, XIII, V of Fig. 1, corresponding to three fixed nematic concentrations. *Dots* on each curve indicate the shear rate where the tumbling to wagging transition occurs

Figure 12 shows the averaged first (N_1) and second (N_2) normal stress differences, as well as the apparent viscosity (η). The dots on those curves indicate the transition between the tumbling and wagging state. One observes these rheological properties change gradually during the **T**–**W** transition as shown also by experiments

(Mewis et al. 1997). However, *we do find that the first normal difference N_1 changes sign (from positive to negative) around this transition point*. The second normal stress difference is primarily positive for both tumbling and wagging states. All these quantities are monotone functions of the Peclet number. From Fig. 4 (dashed line), one also knows that N_1 attains its minimum (negative) and N_2 attains its maximum during the transition from wagging states to tilted kayaking ($\mathbf{K}_2$) states. The transition from **W** to **FA** is characterized by a negative, local minimum value (i.e., the maximum negative value) of N_1, which is consistent with experiments by Mewis et al. (1997) where their conclusion is that transition from **T** to **FA** occurs around the maximum negative value of N_1.

Stable kayaking ($\mathbf{K}_1$) and tilted kayaking ($\mathbf{K}_2$) states

Stable kayaking ($\mathbf{K}_1$) states exist for intermediate concentrations (Regions III, VII, VIII, IX). For fixed concentration and variable *Pe*, the $\mathbf{K}_1$ attractor emerges in two different scenarios. One is an immediate emergence from a quiescent nematic phase in weak shear at nematic but not high concentrations. Another is emergence from the logrolling state by Hopf bifurcation at larger concentrations and above a critical *Pe*. In all cases, $\mathbf{K}_1$ states disappear through a turning point bifurcation as *Pe* increases. *Experimentally*, the kayaking response will simply disappear at a critical *Pe*, and an apparent first-order phase transition will be observed! In actuality, Table 3 explains that one passes from bi-stable (VIII–X) or tri-stable (VII–VI) regimes where $\mathbf{K}_1$ coexists with **W** or $\mathbf{K}_2^{\pm}$ orbits to a regime with only **W** or $\mathbf{K}_2^{\pm}$ attractors.

Paired tilted kayaking states ($\mathbf{K}_2^{\pm}$) arise as *Pe* increases through a pitchfork bifurcation of the wagging branch, and as Peclet decreases through Hopf bifurcations of the out-of-plane steady state pair, shown in Figs. 13 and 9. While these transitions into and out of $\mathbf{K}_1$ orbits are robust, significant differences in the surrounding stable and unstable PDFs are evident from Figs. 13a ($N = 5.05$), 13b ($N = 5.2$), and 9 ($N = 5.5$). *These symmetric $\mathbf{K}_2$ orbits are critical to the period-doubling bifurcation sequence to the chaotic Regions IV and V*. The concentration $N = 5.5$, Fig. 9, suppresses the period-doubling behavior, and thereby suppresses so-called rheochaos. At lower concentrations, $N = 5.05$ (Fig. 13a) and $N = 5.2$ (Fig. 13b), two very different bifurcation scenarios are shown, *both* with period-doubling sequences to chaos.

For stable $\mathbf{K}_1$ and $\mathbf{K}_2$ states, the averaged first (N_1) and second (N_2) normal stress differences, as well as the apparent viscosity (η), are plotted in Figs. 14 and 15, respectively. Compared with tumbling/wagging states, these properties for $\mathbf{K}_1$ states reverse monotonicity as the Peclet number increases. Typically, $N_1(\mathbf{K}_1) > 0$ increases,

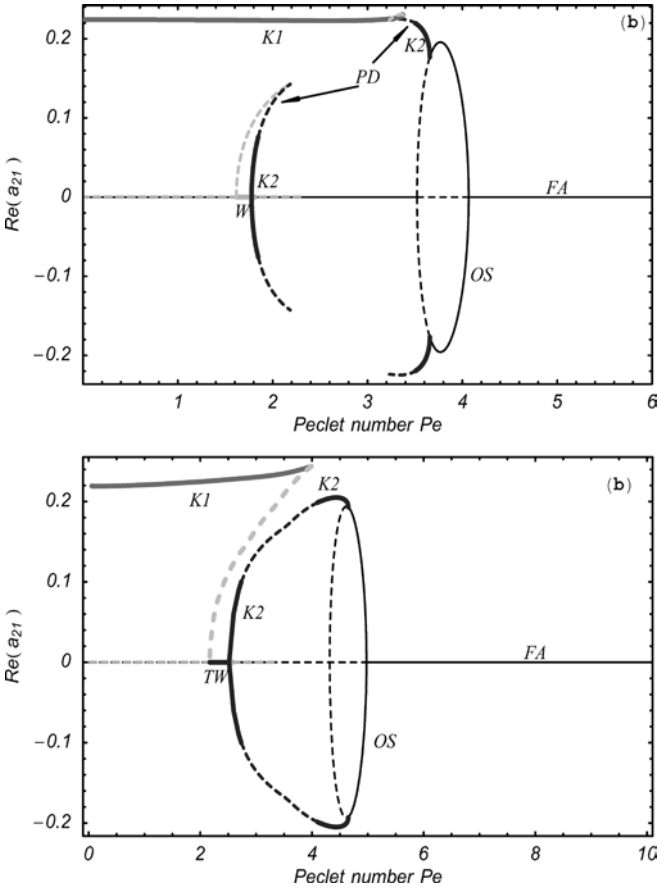

Fig. 13 Subtle differences in the *Pe*-dependent bifurcation sequence as one varies concentration *N*. The *top figure* is the bifurcation diagram for $N = 5.05$, the *bottom figure* is for $N = 5.2$. These differences appear to be important in the dynamical properties of the chaotic attractors (private study by Kevrekidis, Russo and the authors)

while in Region VIII where $\mathbf{K}_1$ states co-exist with the wagging state, $N_1(\mathbf{W}) < 0$ decreases. *This is one rheological difference between in-plane wagging states and out-of-plane kayaking $\mathbf{K}_1$ states, which might be useful to confirm experimentally*. Mostly, but not uniformly, $N_1(\mathbf{K}_2) < 0$. From Fig. 4, both $N_1(\mathbf{K}_2) < 0$ and $N_1(\mathbf{W}) < 0$, but contrary to the stable wagging **W** states, N_1 increases and N_2 decreases for $\mathbf{K}_2$ orbits as the shear rate *Pe* increases. *This Pe-dependent feature may help to distinguish experimentally in-plane wagging states and out-of-plane tilted wagging states*. However, for both $\mathbf{K}_2$ and **W** states, the apparent viscosity η decreases. During the unsteady-steady transition from $\mathbf{K}_2$ to steady **OS** states, N_1attains its maximum, while N_2 and η attain their minimum.

Period doubling and chaos

Chaotic dynamics (in Regions III, IV, Fig. 1) in sheared liquid crystalline polymers has been studied carefully by

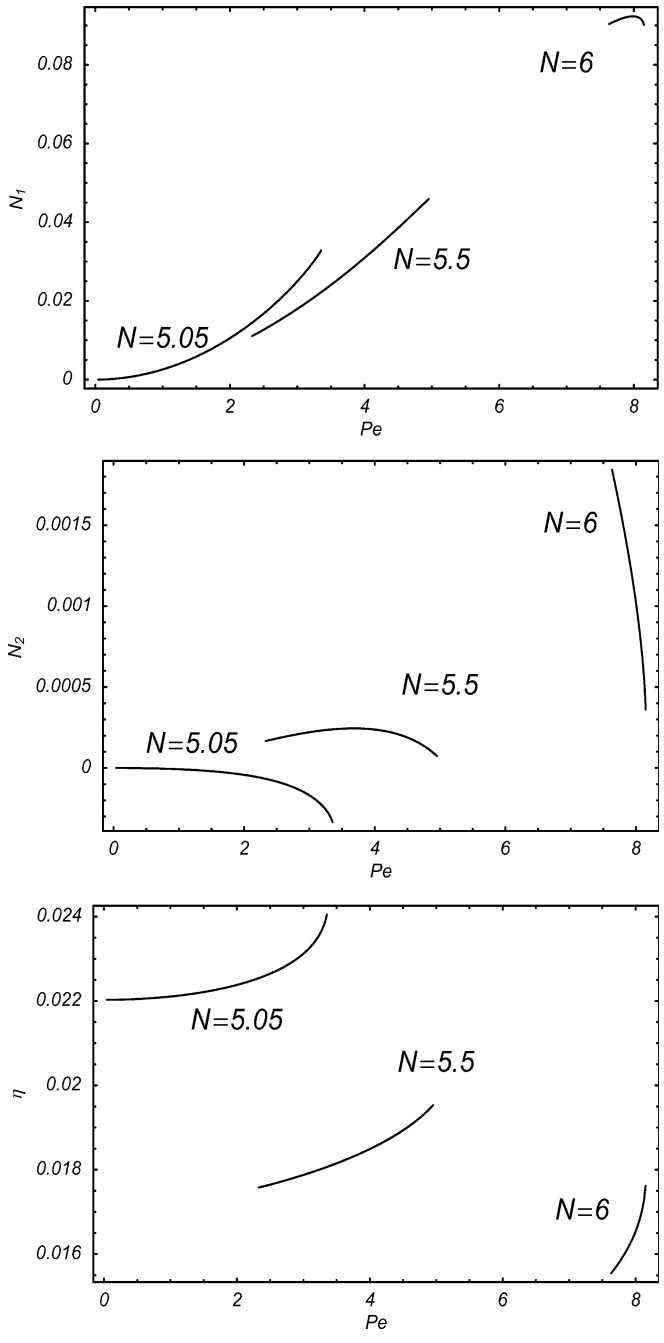

Fig. 14 Time averages of normal stress differences and apparent viscosity for kayaking (K_1) stable states

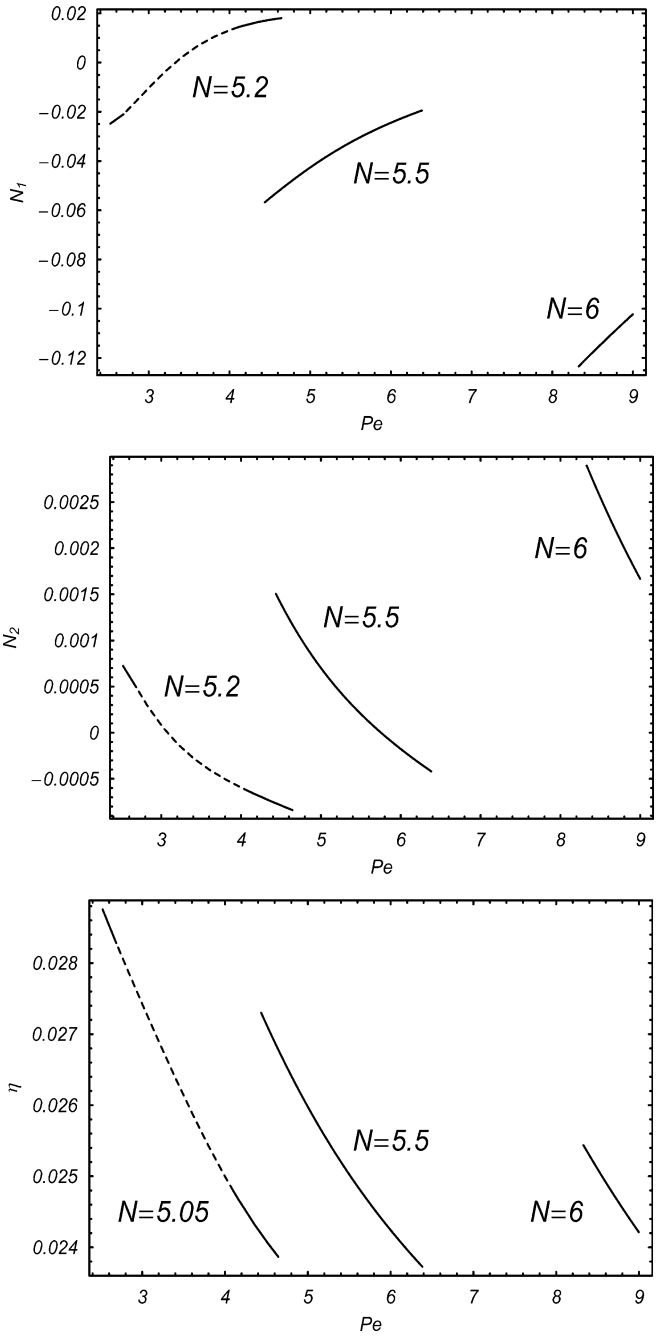

Fig. 15 Average normal stress differences and viscosity for kayaking K_2 stable states (data for the unstable branch for $N = 5.2$ is also shown as *dashed line*)

Grosso et al. (2001) using the kinetic model. Forest and Wang 2003; Rienacker et al. 2002 also give a detailed analysis using mesoscopic models. For completeness, in Fig. 16, we show two period-doubled kayaking $\mathbf{K}_2$ states and a chaotic attractor which results from a period-doubling cascade. The normal stress differences N_1 and N_2 oscillate between positive and negative values for all these attractors. We only report a short time series from the chaotic attractor. On a longer timescale, the major director in fact jumps to cover different patches on the sphere, as shown in mesoscopic simulations (Forest and Wang 2003). A refined study of at least two *distinct* chaotic attractors by Russo, Kevrekidis, and the authors will be reported elsewhere.

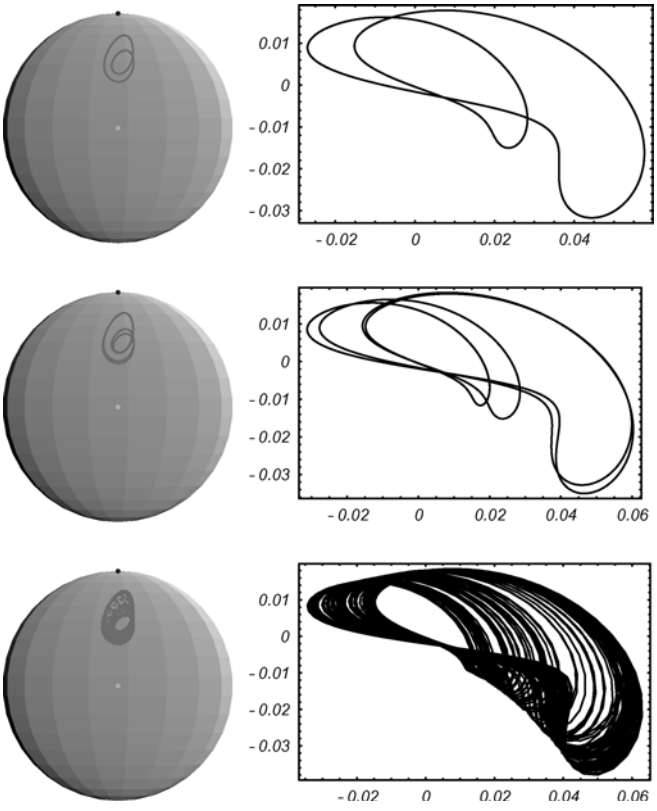

Fig. 16 The period-doubling route to rheochaos for fixed concentration $N = 5.2$ as shear rate decreases, $Pe = 4.07$, 4.05 and 4.044, respectively, from *top to bottom*. *Left figures* show the major director on the sphere, while *right figures* show the rheological phase plot of normal stress differences (N_1, horizontal axis; N_2, vertical axis)

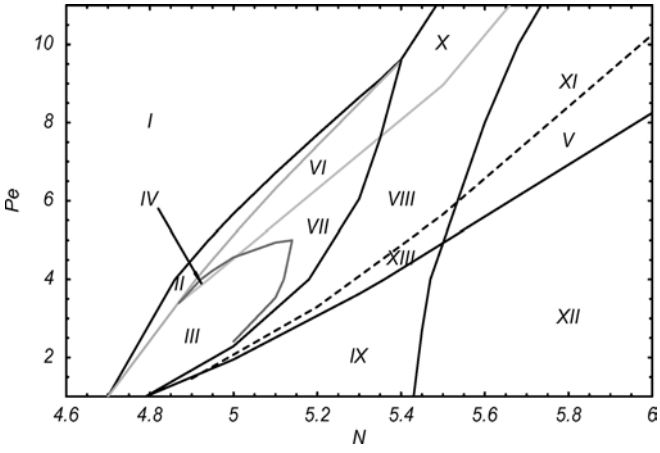

Fig. 17 Flow-phase diagram of the Smoluchowski equation (Eq. 1) with variable orientation-dependent rotational diffusivity. Table 1 lists all attractors for each region I–XIII

Orientation-dependent rotational diffusivity

For completeness, we give the phase diagram with orientation-dependent rotational diffusivity, that is, Eq. (1) with

$$D_r(\mathbf{m}) = D_r^0 \left(\frac{4}{\pi} \int_{||\mathbf{m}'||=1} ||\mathbf{m} \times \mathbf{m}'|| f(\mathbf{m}')\, d\mathbf{m}' \right)^{-2}. \qquad (9)$$

To simplify the calculation, we adopt the strategy used by Larson and Ottinger (1991) to move D_r out of the rotational operator. The phase diagram is shown in Fig. 17. Comparing this phase diagram and the phase diagram in Fig. 1 with constant orientation-dependent rotational diffusivity, we find that these two diagrams are qualitatively the same.

Conclusion

The kinetic phase diagram of Doi-Hess theory for sheared nematic polymer monodomains has been described in detail. This diagram gives the complete set of stable orientational distribution functions vs concentration N and normalized shear rate Pe, together with the myriad of phase transitions. Furthermore, the measurable rheology of each attractor has been presented, together with detectable signatures of phase transitions, and robust features which may guide experimentalists to distinguish the subtle differences between in-plane and out-of-plane limit cycles. We close with a general resumé of the kinetic theory predictions:

- **FA** states exist for any N and sufficiently high Pe. The Leslie alignment angle is small, yet it can be either positive or negative. N_1 is positive for low concentrations yet negative at high concentrations; N_1 increases with Pe in either case. The magnitude of N_2 is small and decreases with Pe. The apparent viscosity η exhibits weak shear thinning.
- For **LR** states, $N_1 > 0$, $N_2 > 0$ and both of them are increasing functions of Pe for any N; η grows only slightly with Pe.
- Out-of-plane steady states $\mathbf{OS}^{\pm}$ only exist in a very narrow band in the (N,Pe) parameter space. The transition between $\mathbf{OS}^{\pm}$ and **FA** states is characterized by a local minimum of N_1 and a local maximum of N_2 and η, while the transition between $\mathbf{OS}^{\pm}$ states and $\mathbf{K}_2$ states is characterized by a local maximum of N_1 and local minimum of N_2 and η.
- For **T/W** states, N_1decreases with Pe and $N_2 > 0$ increases. Generally, $N_1 > 0$ for tumbling states and $N_1 < 0$ for wagging states, that is, the transition from **T** to **W** is loosely characterized by a sign change in N_1.
- From the average apparent viscosity, $\mathbf{K}_1$ states are shear thickening, while $\mathbf{K}_2$ states are shear thinning. For both $\mathbf{K}_1$ and $\mathbf{K}_2$ states, N_1 increases and N_1 decreases as Pe increases, contrary to the in-plane **T/W** states, for which N_1 is decreasing and N_2 is increasing.

– For the chaotic attractors **CH**, N_1 and N_2 oscillate erratically, changing sign frequently.

It is hoped that this resumé of attractors and rheological features can serve as a guide for experimentalists to interpret shear data on nematic polymers. It is further hoped that shortcomings of the Doi-Hess theory may be organized within this framework, so that necessary modifications can be systematically explored. Finally, the myriad transition phenomena pose high hurdles for theorists who aspire to rigorous results on the Doi-Hess-Smoluchowski equation.

Acknowledgement Effort sponsored by the Air Force Office of Scientific Research, Air Force Materials Command, USAF, under grant number F49620-02-1-0086, and the National Science Foundation through grants DMI-0115445, DMS-0204243, DMS-0308019. This work is supported in part by the NASA University Research, Engineering and Technology Institute on Bio Inspired Materials (BIMat) under award No. NCC-1-02037.

Appendix. Second moment projection and stress formula

Suppose the PDF has the following spherical harmonic expansion:

$$f(\mathbf{m},t)=\sum_{l=0}^{\infty}\sum_{m=-l}^{l}a_{l,m}(t)Y_l^m(\theta,\phi), \tag{A1}$$

where Y_l^m are complex spherical harmonic functions. The five independent components of the second moment tensor $\mathbf{Q}$ can be expressed as

$$Q_{xx}=-\frac{2}{3}\sqrt{\frac{\pi}{5}}a_{2,0}+\sqrt{\frac{8\pi}{15}}\Re(a_{2,2}) \tag{A2}$$

$$Q_{yy}=-\frac{2}{3}\sqrt{\frac{\pi}{5}}a_{2,0}-\sqrt{\frac{8\pi}{15}}\Re(a_{2,2}) \tag{A3}$$

$$Q_{xy}=-\sqrt{\frac{8\pi}{15}}\Im(a_{2,2}) \tag{A4}$$

$$Q_{xz}=-\sqrt{\frac{8\pi}{15}}\Re(a_{2,1}) \tag{A5}$$

$$Q_{yz}=\sqrt{\frac{8\pi}{15}}\Im(a_{2,1}) \tag{A6}$$

where, $\Re(\cdot)$ and $\Im(\cdot)$ represent the real and the imaginary part of the number respectively.

The extra stress in dimensional form is given by (Wang 2002)

$$\begin{aligned}\tau=&(\eta_0+3\nu kT\,\zeta_3)\mathbf{D}+3\,a\,\nu kT\,[\mathbf{Q}-N(\mathbf{Q}+\frac{\mathbf{I}}{3})\mathbf{Q}+N\mathbf{Q}\\&:\langle\mathbf{mmmm}\rangle]+3\nu kT\,[\zeta_1(\mathbf{DM}+\mathbf{MD})+\zeta_2\mathbf{D}:\mathbf{M}_4],\end{aligned} \tag{A7}$$

where, η_0 is the isotropic viscosity, ζ_0 is a free parameter determined experimentally, ν is the molecule number density, and all other parameters are prescribed by the molecule aspect ratio r:

$$\begin{aligned}&\zeta_3=\tfrac{\zeta^{(0)}}{I_1},\zeta_1=\zeta^{(0)}(\tfrac{1}{I_3}-\tfrac{1}{I_1}),\zeta_2=\zeta^{(0)}[\tfrac{J_1}{I_1J_3}+\tfrac{1}{I_1}-\tfrac{2}{I_3}],\\&I_1=2r\textstyle\int_0^\infty\frac{dx}{\sqrt{(r^2+x)(1+x)^3}},I_3=r(r^2+1)\int_0^\infty\frac{dx}{\sqrt{(r^2+x)}(1+x)^2(r^2+x)},\\&J_1=r\textstyle\int_0^\infty\frac{xdx}{\sqrt{(r^2+x)(1+x)^3}},J_3=r\int_0^\infty\frac{xdx}{\sqrt{(r^2+x)}(1+x)^2(r^2+x)}.\end{aligned} \tag{A8}$$

In our calculations, we have used values $\zeta_1=0$, $\zeta_2=0.1$, $\zeta_3=0.001$, consistent with extremely large aspect ratio rod-like nematic polymers, $r\gg1$. For the fourth moment tensor $\langle\mathbf{mmmm}\rangle$ we do not use any closure rule. The exact calculation of this tensor can be found in the Appendix in Forest et al. (2004b).

The first and second normal stress differences N_1 and N_2, and the apparent viscosity η are computed as

$$\begin{aligned}N_1&=\tau_{xx}-\tau_{yy},\\N_2&=\tau_{yy}-\tau_{zz},\\\eta&=\tau_{xy}/Pe.\end{aligned} \tag{A9}$$

All these quantities are normalized by $3\nu kT$.

References

Bird B, Armstrong RC, Hassager O (1987) Dynamics of polymeric liquids, vols 1 and 2. John Wiley and Sons

Burghardt WR (1998) Molecular orientation and rheology in sheared lyotropic liquid crystalline polymers. Macromol Chem Phys 471–488

Doedel EJ, Champneys AR, Fairgrieve TF, Kuznetsov YA, Sandstede B, Wang X (1997) AUTO97: continuation and bifurcation software for ordinary differential equations. Concordia University

Doi M (1981) Molecular dynamics and rheological properties of concentrated solutions of rodlike polymers in isotropic and liquid crystalline phases. J Polym Sci Polym Phys Ed 229–243

Faraoni V, Grosso M, Crescitelli S, Maffettone PL (1999) The rigid-rod model for nematic polymers: an analysis of the shear flow problem. J Rheol 829–843

Forest MG, Wang Q (2003) Monodomain response of finite-aspect-ratio macromolecules in shear and related linear flows. Rheol Acta 20–46

Forest MG, Zhou R, Wang Q (2002) Symmetries of the Doi kinetic theory for nematic polymers of arbitrary aspect ratio: at rest and in linear flows. Phys Rev E 3:031712

Forest MG, Wang Q, Zhou R (2004a) The weak shear kinetic phase diagram for nematic polymers. Rheol Acta 17–37

Forest MG, Zhou R, Wang Q (2004b) Scaling behavior of kinetic orientational distributions for dilute nematic polymers in weak shear. J Non-Newtonian Fluid Dynamics 183–204

Grosso M, Keunings R, Crescitelli S, Maffettone PL (2001) Prediction of chaotic dynamics in sheared liquid crystalline polymers. Phys Rev Lett 14:3184–3187

Hess S (1976) Fokker-Planck-equation approach to flow alignment in liquid crystals. Z Naturforsch Teil A 1034–1037

Larson RG (1990) Arrested tumbling in shearing flows of liquid crystal polymers. Macromolecules 3983–3992

Larson RG, Ottinger H (1991) The effect of molecular elasticity on out-of-plane orientations in shearing flows of liquid crystalline polymers. Macromolecules 6270–6282

Mewis J, Mortier M, Vermant J, Moldenaers P (1997) Experimental evidence for the existence of a wagging regime in polymeric liquid crystals. Macromolecules 1323–1328

Rienacker G, Kroger M, Hess S (2002) Chaotic and regular shear-induced orientational dynamics of nematic liquid crystals. Physica A 537–568

Wang Q (2002) A hydrodynamic theory for solutions of nonhomogeneous nematic liquid crystalline polymers of different configuration. J Chem Phys 20:9120–9136